



Proceedings of the XXVII Iberian Latin American Congress on
Computational Methods in Engineering
September 3 to 6, 2006 - Belém, Pará - BRAZIL.

DIRECT SIMULATION OF RAREFACTION EFFECT ON POWER-LAW LEADING EDGES IN HYPERSONIC FLOW

Wilson F. N. Santos

wilson@lcp.inpe.br

Combustion and Propulsion Laboratory
National Institute for Space Research
Cachoeira Paulista, SP, 12630-000, BRAZIL

***Abstract.** This work deals with a numerical study of power-law leading edges situated in a hypersonic flow. The primary aim of this paper is to examine the effect of rarefaction on the aerodynamic surface quantities. Rarefaction effect on the aerodynamic surface quantities has been investigated by employing the Direct Simulation Monte Carlo (DSMC) method. The work is motivated by interest in investigating power-law shaped leading edges as possible candidates for blunting geometry of hypersonic leading edges. The sensitivity of aerodynamic heating and drag to variations on rarefaction are simulated for altitudes of 70, 80 and 85 km. The analysis shows significant differences on the aerodynamic heating and drag due to variations not only on the altitude but also on the leading-shape defined by the power-law exponent. It was found that the heat transfer and drag coefficients increase with increasing the altitude.*

Keywords: Hypersonic flow, Rarefied flow, DSMC, Power-law shape, Aerodynamic heating.

1. INTRODUCTION

Hypersonic waverider configurations have been proposed as promising airframes for high-speed vehicles because they have the highest known lift-drag (L/D) performance. A waverider concept, introduced by Nonweiler (1959), is a lifting body that is derived from a known analytical flowfield, such as a flow over a two-dimensional wedge or a flow over a slender cone. The potential for high L/D ratio on waveriders originates from the high-pressure region between the shock wave and the lower surface. Due to the sharp leading edge, the attached shock wave prevents the high-pressure gas from the lower surface to communicate with the gas on the upper surface. However, as any practical waverider will have some degree of leading edge bluntness for heat transfer, manufacturing and handling concerns, then the predicted performance of waverider configurations may not be achieved. Moreover, because of the viscous effects, the shock wave will be detached from the leading edge and, hence, the aerodynamic performance of the vehicle may be degraded from ideal performance. Typically, a round leading edge with constant radius of curvature near the stagnation point (circular cylinder) has been chosen. Nevertheless, shock detachment distance on a cylinder, with associated leakage, scales with the radius of curvature.

Certain classes of non-circular shapes, such as power-law shaped leading edges ($y \propto x^n$, $0 < n < 1$), may provide the required bluntness for heat transfer, manufacturing and handling concerns with reduced departures from ideal aerodynamic performance. This concept is based on work of Mason and Lee (1994), who have pointed out, based on Newtonian flow analysis, that power-law shapes exhibit both blunt and sharp aerodynamic properties. They suggested the possibility of a difference between shapes that are geometrically sharp and shapes that behave aerodynamically as if they were sharp.

Based on recent interest in hypersonic waveriders for high-altitude/low-density applications (Anderson, 1990, Potter and Rockaway, 1994, Rault, 1994, Graves and Argrow, 2001, Shvets et al., 2005), Santos and Lewis (2002a, 2002b, 2003, 2005a and 2005b) has investigated the effect of the power-law exponent on the flowfield structure over these leading edges. The power-law exponent effect on shock-wave structure was examined by Santos (2004a, 2004b and 2005). The major interest in these works has gone into considering the power-law body as possible candidate for blunting geometries of hypersonic leading edges.

In an effort to obtain further insight into the nature of the aerodynamic surface quantities of power-law leading edges under hypersonic transitional flow conditions, a parametric study is performed on these shapes with a great deal of emphasis placed on the rarefaction effects. In this scenario, the primary goal of this paper is to assess the sensitivity of the aerodynamic heating and total drag to variations not only on the rarefaction experienced by the leading edges but also on the shape of the leading edges via power-law exponent.

For the high altitude/high Knudsen number of interest ($Kn > 0.1$), the flowfield is sufficiently rarefied that continuum method becomes inappropriate. Alternatively, the DSMC method is used in the current study to calculate the rarefied hypersonic two-dimensional flow on the leading edge shapes.

2. LEADING-EDGE GEOMETRY

In dimensional form, the body power-law shapes are given by the following expression,

$$y = ax^n \tag{1}$$

where n is the power-law exponent and a is the power-law constant which is a function of n .

The power-law shapes are modeled by assuming a sharp leading edge of half angle θ with

a circular cylinder of radius R inscribed tangent to this wedge. The power-law shapes, inscribed between the wedge and the cylinder, are also tangent to them at the same common point where they have the same slope angle. The circular cylinder diameter provides a reference for the amount of blunting desired on the leading edges. It was assumed a leading edge half angle of 10 degrees, a circular cylinder diameter of 10^{-2} m and power-law exponents of 1/2, 2/3, and 3/4. Figure 1(a) illustrates schematically this construction for the set of power-law leading edges investigated.

From geometric considerations, the power-law constant a is obtained by matching slope on the wedge, circular cylinder and power-law body at the tangency point. The common body height H at the tangency point is equal to $2R\cos\theta$, and the body length L from the nose to the tangency point in the axis of symmetry is given by $nH/2\tan\theta$. It was assumed that the power-law leading edges are infinitely long but only the length L is considered since the wake region behind the power-law bodies is not of interest in this investigation.

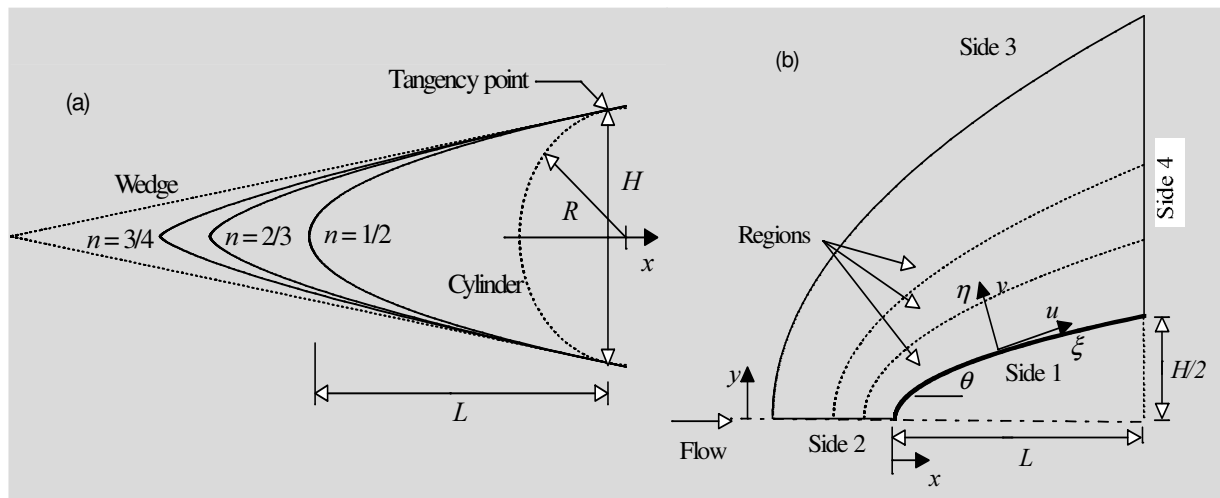


Figure 1: Drawing illustrating (a) the leading edge shapes and (b) the computational domain.

3. COMPUTATIONAL TOOL

The DSMC method (Bird, 1994) has proved to be an extremely useful and flexible tool in the analysis of rarefied hypersonic non-equilibrium gas flows. In this study, the particle simulations were performed by using the DSMC method developed by Bird (1994). The DSMC method simulates fluid flow by using thousands to millions of particles. These particles are tracked as they move, collide and undergo boundary interactions in simulated physical space. In addition, particle motions are assumed to be decoupled from particle collisions and each process is computed independently during a time step used to advance the simulation. This time step must be sufficiently small in comparison with the local mean collision time (Garcia and Wagner, 2000, and Hadjiconstantinou, 2000) such that the assumption of decoupled particle motions and collisions is not violated.

The reliability of the method is entirely dependent on the accuracy of the collision models used to simulate particles interactions. The molecular collisions are modeled using the variable hard sphere (VHS) molecular model (Bird, 1981) and the no time counter (NTC) collision sampling technique (Bird, 1989). The VHS model employs the simple hard sphere angular scattering law so that all directions are equally possible for post-collision velocity in the center-of-mass frame of reference. However, the collision cross section is a function of the relative energy in the collision. The energy exchange between kinetic and internal modes is controlled by the Borgnakke-Larsen statistical model (Borgnakke and Larsen, 1975).

Simulations are performed using a non-reacting gas model consisting of two chemical species, N_2 and O_2 . Energy exchanges between the translational and internal modes are considered. For this study, the relaxation numbers of 5 and 50 were used for the rotation and vibration, respectively.

4. COMPUTATIONAL FLOW DOMAIN AND GRID

The computational domain is made large enough so that the upstream and side boundaries can be specified as freestream conditions. Figure 1(b) depicts the physical extent of the computational domain for the present simulations. Advantage of the flow symmetry is taken into account, and molecular simulation is applied to one-half of a full configuration. The computational domain is divided into an arbitrary number of regions, which are subdivided into computational cells. The cells are further subdivided into four subcells, two subcells/cell in each coordinate direction. The linear dimensions of the cells should be small in comparison with the scale length of the macroscopic flow gradients normal to the streamwise directions, which means that the cell dimensions should be of the order of or even smaller than the local mean free path (Alexander et al., 1998 and 2000). In the current DSMC code, the cell provides a convenient reference for the sampling of the macroscopic gas properties, while the collision partners are selected from the same subcell. As a result, the flow resolution is much higher than the cell resolution.

Referring to Fig. 1(b), side 1 is defined by the body surface. Diffuse reflection with complete thermal surface accommodation is the condition applied to this side. Side 2 is a plane of symmetry, where all flow gradients normal to the plane are zero. At the molecular level, this plane is equivalent to a specular reflecting boundary. Side 3 is the freestream side through which simulated molecules enter and exit. Finally, the flow at the downstream outflow boundary, side 4, is predominantly supersonic and vacuum condition is specified (Guo and Liaw, 2001). At this boundary, simulated molecules can only exit.

Numerical accuracy in DSMC method depends on the grid resolution chosen as well as on the number of particles per computational cell. Both effects were investigated to determine the number of cells and the number of particles required to achieve grid independence solutions.

The grid generation scheme used in this study follows that procedure presented by Bird (1994). Along the outer boundary (side 3) and the body surface (side 1) (see Fig. 1(b)), point distributions are generated in such way that the number of points on each side is the same (ξ -direction in Fig. 1(b)). Then, the cell structure is defined by joining the corresponding points on each side by straight lines and then dividing each of these lines into segments which are joined to form the system of quadrilateral cells (η -direction in Fig. 1(b)). The distribution can be controlled by a number of different distribution functions that allow the concentration of points in regions where high flow gradients or small mean free paths are expected.

A grid independence study was made with three different structured meshes in each coordinate direction. The effect of altering the cell size in the ξ -direction was investigated with grids of 35(coarse), 70(standard) and 105(fine) cells, and 50 cells in the η -direction for power-law exponent of 1/2. In analogous fashion, an examination was made in the η -direction with grids of 25(coarse), 50(standard) and 75(fine) cells, and 70 cells in the ξ -direction for power-law exponent of 1/2. Each grid was made up of non-uniform cell spacing in both directions. The effect (not shown) of changing the cell size in both directions on the heat transfer, pressure and skin friction coefficients was rather insensitive to the range of cell spacing considered, indicating that the standard grid, 70x50 cells, for the power-law shape defined by $n = 1/2$ is essentially grid independent. A similar procedure was performed for the two other cases investigated. Results indicated that a grid of 80x50 and 90x50 for power-law

exponents of 2/3 and 3/4 respectively, were considered fully independent. Of particular interest is the number of cells in the η -direction for the three power-law cases investigated. It should be emphasized that, even though the number of cells is the same, the computational domain size is different for each one of the cases; side 2 shown in Fig. 1(b) corresponds to $8\lambda_\infty$, $6\lambda_\infty$ and $5\lambda_\infty$ for power-law exponents of 1/2, 2/3 and 3/4, respectively, where λ_∞ is the freestream mean free path.

In a second stage of the grid independence investigation, a similar examination was made for the number of molecules. The standard grid for power-law exponent of 1/2, 70x50 cells, corresponds to, on average, a total of 121,000 molecules. Two new cases using the same grid, were investigated. These two new cases correspond to 108,000 and 161,000 molecules in the entire computational domain. As the three cases presented approximately the same results (see Santos and Lewis, 2005) for the heat transfer, pressure and skin friction coefficients, hence the standard grid with a total of 121,000 molecules is considered enough for the computation of the aerodynamic surface quantities.

5. FREESTREAM AND FLOW CONDITIONS

The freestream and flow conditions used in the present calculations are those given by Santos (2001) and summarized in Table 1. The gas properties considered in the simulation are those given by Bird (1994) and tabulated in Table 2.

Referring to Tables 1 and 2, T_∞ , p_∞ , ρ_∞ , n_∞ , μ_∞ , and λ_∞ stand respectively for temperature, pressure, density, number density, viscosity and mean free path, and X , m , d and ω account respectively for mole fraction, molecular mass, molecular diameter and viscosity index.

Table 1: Freestream Conditions

Altitude (km)	T_∞ (K)	p_∞ (N/m ²)	$\rho_\infty \times 10^5$ (kg/m ³)	$n_\infty \times 10^{-20}$ (m ⁻³)	$\mu_\infty \times 10^5$ (Ns/m ²)	$\lambda_\infty \times 10^3$ (m)	V_∞ (m/s)
70	220.0	5.582	8.753	18.2090	1.455	0.903	3560
80	181.0	1.040	1.999	4.1586	1.253	3.960	3236
85	181.0	0.414	0.796	1.6550	1.253	9.940	3236

Table 2: Gas Properties

	X	m (kg)	d (m)	ω
O ₂	0.237	5.312×10^{-26}	4.01×10^{-10}	0.77
N ₂	0.763	4.65×10^{-26}	4.11×10^{-10}	0.74

Rarefaction effects are investigated for altitude of 70, 80 and 85 km. For each one of the altitude investigated, the freestream Mach number M_∞ and the wall temperature T_w are kept to the constant values of 12 and 880 K, respectively. Freestream Mach number M_∞ of 12 corresponds to freestream velocity V_∞ of 3.56, 3.236 and 3.236 km/s for altitude of 70, 80 and 85 km, respectively.

The overall Knudsen number Kn_∞ , defined as the ratio of the freestream mean free path λ_∞ to the diameter of the circular cylinder, corresponds to 0.0903, 0.3960 and 0.9940 for altitude of 70, 80 and 85 km, respectively. Finally, the Reynolds number Re_∞ per unit of meter, based on conditions in the undisturbed stream is 21416.3, 5165 and 2055 for altitude of 70, 80 and 85 km, respectively

6. COMPUTATIONAL RESULTS AND DISCUSSION

The degree of rarefaction is measured by the Knudsen number. This parameter may also be interpreted as defining the importance of the effect of molecular motions on the flowfield. When the Knudsen number is small, say less than 0.1, the effect of molecular motions on the flow is negligible and, in this regime the gas can be treated as a continuous medium. For large values of the Knudsen number, of the order of 10, the effect of molecular motions is important and the phenomena that occur can be completely described in terms of the motions of individual molecules, defining the free molecular regime. By virtue of the well-established laws of molecular motions, flows in the free molecular regime are readily investigated analytically. The regime of intermediate Knudsen numbers ($0.1 < Kn < 10$) which is difficult to treat analytically is simulated in this research by $Kn_\infty = 0.0903$, 0.3960 and 0.9940 , which correspond to the altitude of 70, 80 and 85 Km, respectively. Therefore, this section focuses on the effects that take place on the aerodynamic surface quantities due to changes on the altitude as well as on the leading-edge shape. Aerodynamic surface quantities of particular interest in the transitional flow regime are number flux, heat transfer, wall pressure, wall shear stress and drag. In this scenario, this section will discuss and compare differences of these quantities expressed in dimensionless coefficient form.

6.1 Number flux

The number flux N is calculated by sampling the molecules impinging on the surface by unit time and unit area. The dependence of the number flux on rarefaction is illustrated in Figs. 2(a-c) for power-law exponent n of $1/2$, $2/3$ and $3/4$, respectively, as a function of the arc length along the body surface. In this set of figures, the number flux N is normalized by $n_\infty V_\infty$, where n_∞ is the freestream number density and V_∞ is the freestream velocity. Also, the arc length s along the body surface, measured from the stagnation point, is normalized by the radius R of the reference circular cylinder (see Fig. 1). For comparison purpose, the dimensionless number flux predicted by the free molecular flow (FM) equations (Bird, 1994) is also presented.

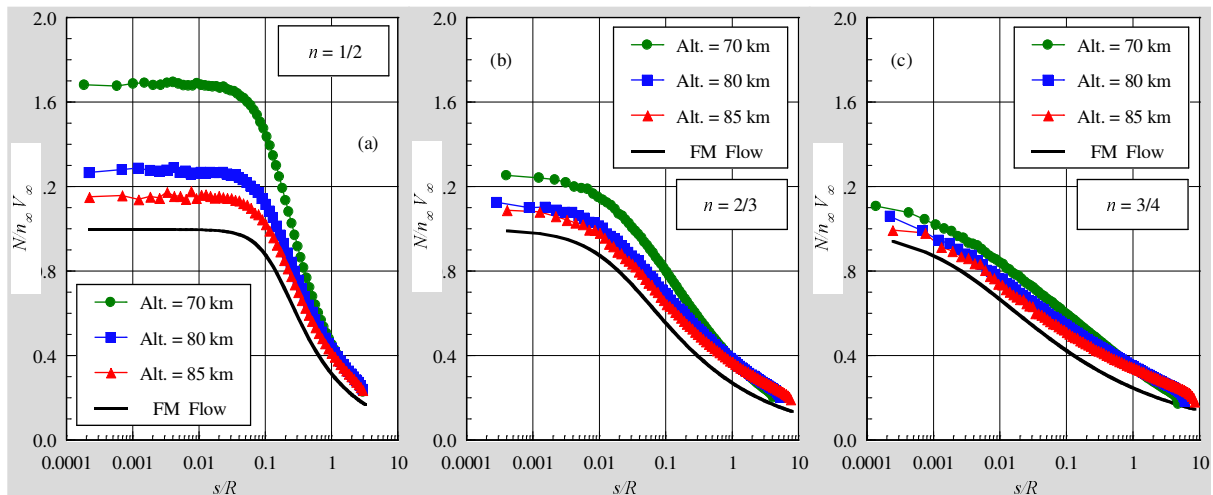


Figure 2: Effect of rarefaction on dimensionless number flux ($N/n_\infty V_\infty$) along the body surface for power-law exponent n of (a) $1/2$, (b) $2/3$ and (c) $3/4$.

According to Figs. 2(a-c), the DSMC results show the qualitative behavior expected in that the dimensionless number flux decreases with increasing rarefaction. Furthermore, the

DSMC calculations follow the same trend of those predicted by the free molecular flow equations. The variation of the dimensionless number flux caused by rarefaction seems to be more pronounced for blunt leading edges ($n \rightarrow 1/2$), and almost vanishes for aerodynamically sharp leading edges ($n \rightarrow 3/4$) for the flow conditions considered in these simulations. The dimensionless number flux predicted by the free molecular flow approaches a value of 1.0 at the stagnation point, as shown for the $n = 1/2$ case. For the $n = 3/4$ case, the dimensionless number flux, that also approaches a value of 1.0 at the stagnation point, drops off to a value around 0.9 into an extremely small length, i.e., $0 \leq s/R \leq 0.0001$. In this small region the body slope angle dramatically decreases from 90 degrees to 70 degrees.

6.2 Heat transfer coefficient

The heat transfer coefficient C_h is defined as being,

$$C_h = \frac{q_w}{\frac{1}{2} \rho_\infty V_\infty^3} \quad (2)$$

where the heat flux q_w to the body surface is calculated by the net energy flux of the molecules impinging on the surface. A flux is regarded as positive if it is directed toward the surface. The heat flux q_w is related to the sum of the translational, rotational and vibrational energies of both incident and reflected molecules as defined by,

$$q_w = q_i + q_r = \sum_{j=1}^N \left\{ \left[\frac{1}{2} m_j c_j^2 + e_{Rj} + e_{Vj} \right]_i + \left[\frac{1}{2} m_j c_j^2 + e_{Rj} + e_{Vj} \right]_r \right\} \quad (3)$$

where N is the number of molecules colliding with the surface by unit time and unit area, m is the mass of the molecules, c is the velocity of the molecules, e_R and e_V stand for the rotational and vibrational energies, and subscripts i and r refer to incident and reflected molecules.

The heat flux was based upon the gas-surface interaction model of fully accommodated, completely diffuse re-emission. This is the most common model assumed, even though it is well known that some degree of specular re-emission and less than complete accommodation are more realistic assumptions. Moreover, it should also be mentioned in this context that the diffuse model assumes that molecules are reflected equally in all directions, quite independently of their incident speed and direction. Due to the diffuse reflection model, the reflected thermal velocity of the molecules impinging on the surface is obtained from a Maxwellian distribution that takes into account for the temperature of the body surface. In this fashion, as the wall temperature is the same for all the cases investigated, the number of molecules impinging on the surface plays the important role on the reflected contribution to the net heat flux to the body surface.

Distributions of net heat transfer coefficient C_h along the body surface are demonstrated in Figs. 3(a-c) for power-law exponent n of 1/2, 2/3 and 3/4, respectively, with altitude as a parameter. In this set of figures, the net heat transfer coefficient data are bounded by the free molecular value. Referring to Figs. 3(a-c), it is clearly seen that altering the altitude produces a substantial change in the heat transfer coefficient provided that the gas-surface interaction is diffuse, as was assumed for the altitude range investigated. As would be expected, the blunter the leading edge is the lower the heat transfer coefficient at the stagnation point. Significant changes are observed for the leading edge cases shown. For the aerodynamically sharp leading edge case, $n = 3/4$, the heat transfer coefficient approaches the free molecular value in the vicinity of the leading edges with increasing rarefaction. In addition, for the bluntest case

investigated, $n = 1/2$, the heat transfer coefficient follows the same trend of that predicted by free molecular flow.

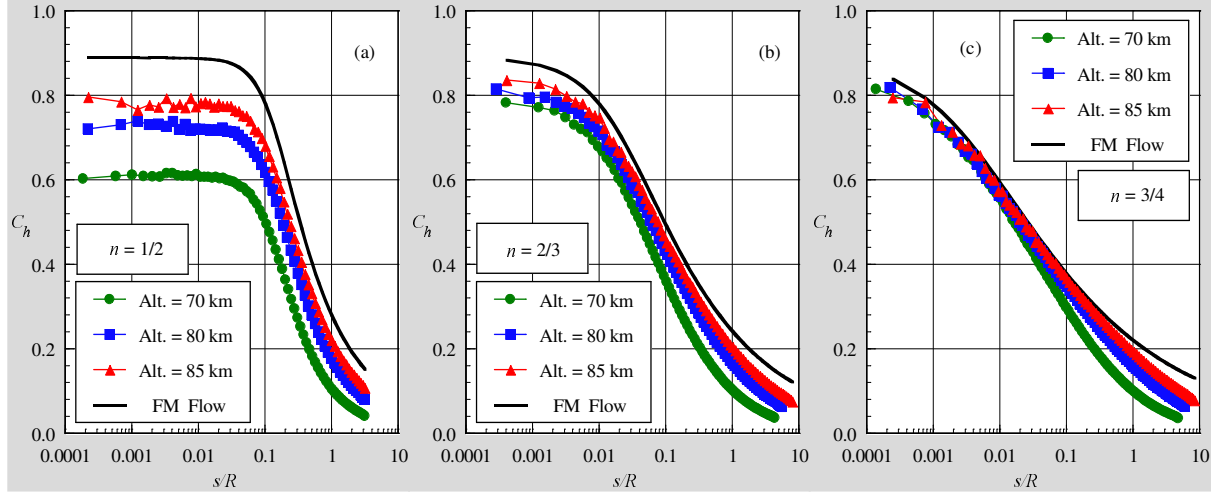


Figure 3: Effect of rarefaction on heat transfer coefficient C_h along the body surface for power-law exponent n of (a) $1/2$, (b) $2/3$ and (c) $3/4$.

6.3 Pressure coefficient

The pressure coefficient C_p is defined as being,

$$C_p = \frac{p_w - p_\infty}{\frac{1}{2} \rho_\infty V_\infty^2} \quad (4)$$

where p_w is the pressure acting on the body surface and p_∞ is the freestream pressure.

The pressure p_w on the body surface is calculated by the sum of the normal momentum fluxes of both incident and reflected molecules at each time step as follows,

$$p_w = p_i + p_r = \sum_{j=1}^N \{ [m_j c_{\eta j}^2]_{\downarrow} + [m_j c_{\eta j}^2]_{\uparrow} \} \quad (5)$$

where c_η is the normal velocity component (η -direction in Fig. 1(b)) of the molecules.

The variation of the pressure coefficient C_p caused by rarefaction effects is shown in Figs. 4(a-c) for power-law exponent n of $1/2$, $2/3$ and $3/4$, respectively. This set of diagrams also shows the pressure coefficient predicted by the free molecular flow. It is noticed that the pressure coefficient presents the expected behavior in that it increases in the vicinity of the stagnation point and tends to the pressure coefficient predicted by the free molecular flow assumption with increasing the altitude. Nevertheless, it is important to mention that this pressure coefficient rise is not attributed to a pressure rise on the body surface. Based on Eq. (5), the wall pressure decreases along the body surface, since the rarefaction causes a decrease in the number of molecules impinging on the body surface (see Figs. 2(a-c)). Therefore, the significant variations shown result from the freestream density used in the normalization of C_p , appearing in Eq. (4), which decreases as the altitude increases from 70 to 85 km.

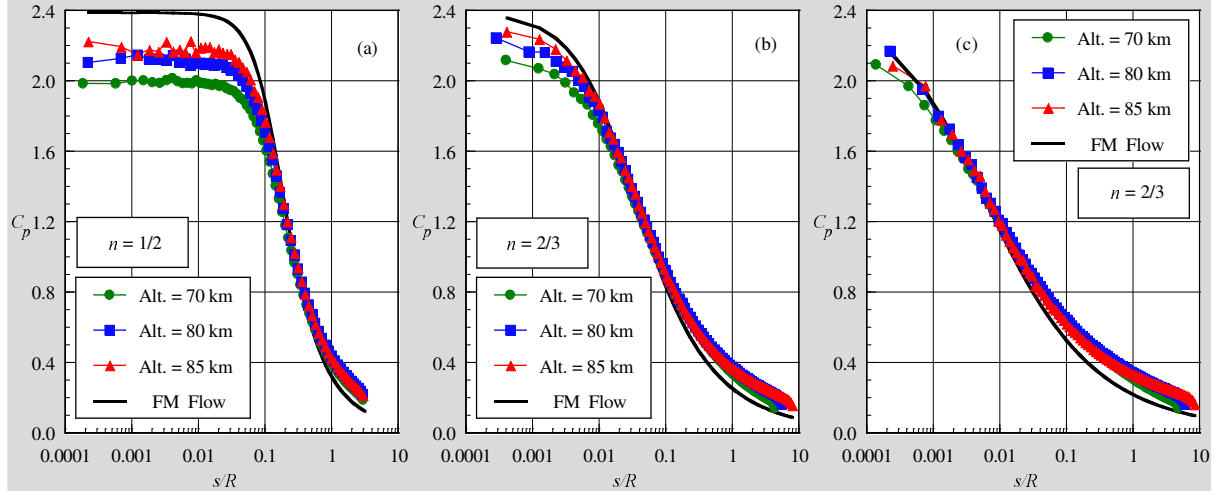


Figure 4: Effect of rarefaction on pressure coefficient C_p along the body surface for power-law exponent n of (a) $1/2$, (b) $2/3$ and (c) $3/4$.

6.4 Skin friction coefficient

The skin friction coefficient C_f is defined as being,

$$C_f = \frac{\tau_w}{\frac{1}{2} \rho_\infty V_\infty^2} \quad (6)$$

where τ_w is the shear stress acting on the body surface.

The shear stress τ_w on the body surface is calculated by the sum of the tangential momentum fluxes of both incident and reflected molecules at each time step as follows,

$$\tau_w = \tau_i + \tau_r = \sum_{j=1}^N \left\{ [m_j c_{\xi_j}^2]_i + [m_j c_{\xi_j}^2]_r \right\} \quad (7)$$

where c_ξ is the tangential component (ξ -direction in Fig. 1(b)) of the molecular velocity.

For the diffuse reflection model imposed for the gas-surface interaction, reflected molecules have a tangential moment equal to zero, since the molecules essentially lose, on average, their tangential velocity component. In this fashion, the second term on the right-hand side of Eq. (7) disappears, and the wall shear stress τ_w reduces to the following expression,

$$\tau_w = \tau_i = \sum_{j=1}^N \left\{ [m_j c_{\xi_j}^2]_i \right\} \quad (8)$$

The extent of the changes in the skin friction coefficient C_f with increasing altitude is presented in Figs. 5(a-c) for power-law exponent n of $1/2$, $2/3$ and $3/4$, respectively. It is found that, contrary to either pressure or heat transfer coefficient, the skin friction coefficient is very sensitive to rarefaction effects for the power-law shapes investigated, tending to the free molecular value with increasing the altitude. The skin friction coefficient is zero at the stagnation point and increases along the body surface up to a maximum value that depends on the leading-edge shape, and then decreases downstream along the body surface. For $n = 2/3$

and 3/4 cases, the skin friction coefficient dramatically increases from zero to the values shown in a small region defined by $0 \leq s/R \leq 0.0001$. As the power-law exponent n increases, the peak value for the skin friction coefficient increases. Also, as the power-law exponent n increases, the peak value is displaced to near the stagnation point.

The skin friction coefficient predicted by the free molecular flow equations exhibits its maximum value at a station that corresponds to a body slope of 45 degrees. Similarly, the maximum values for the power-law exponents investigated occur very close to the same station. An understanding of this behavior can be gained as follows. Based on Figs. 2(a-c), the number of molecules by unit time and unit area impinging on the body surface is high on the stagnation region of the leading edge and low on the body surface far from the stagnation point. In contrast, the tangential velocity component of the molecules is basically zero at the stagnation region and high along the body surface far from the nose of the leading edges due to the flow expansion along the body surface, where the velocities of the molecules are those that are more characteristic of the freestream velocity. As a result, the product of both properties, which is proportional to the skin friction coefficient, presents the maximum value around a station corresponding to 45 degrees. Furthermore, attention should be paid to the fact that a body slope of 45 degrees corresponds to different dimensionless arc length s/R for the leading edges investigated.

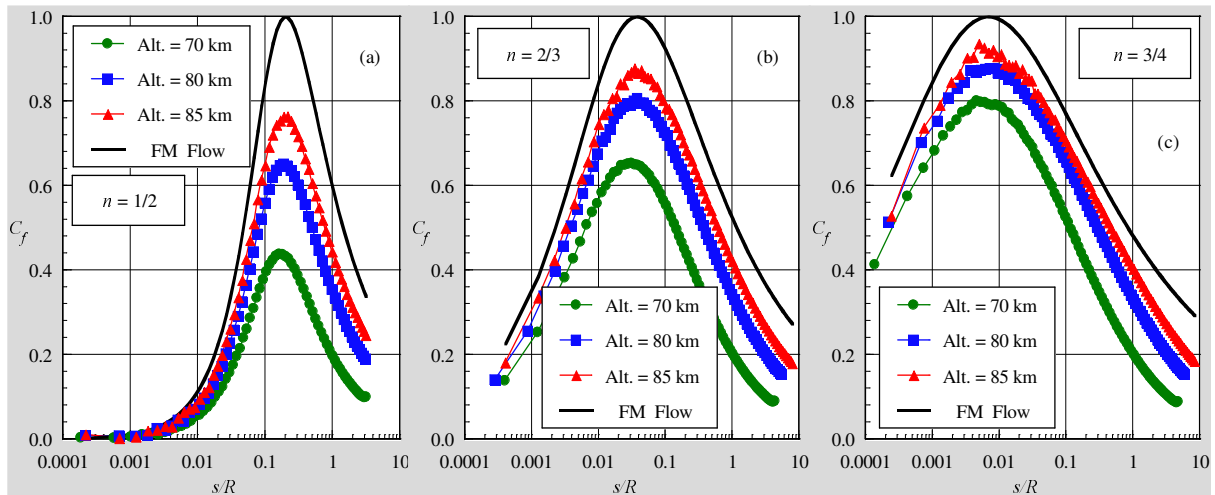


Figure 5: Effect of rarefaction on skin friction coefficient C_f along the body surface for power-law exponent n of (a) 1/2, (b) 2/3 and (c) 3/4.

6.5 Drag coefficient

The total drag coefficient C_d is defined as being,

$$C_d = \frac{F}{\frac{1}{2} \rho_{\infty} V_{\infty}^2 H} \quad (9)$$

where F is the resultant force acting on the body surface, and H is the height at the matching point common to the leading edges (see Fig. 1(b)).

The drag on a surface in a gas flow results from the interchange of momentum between the surface and the molecules colliding with the surface. In this way, the total drag F is obtained by the integration of the pressure p_w and shear stress τ_w distributions from the stagnation point of the leading edges to the station L that corresponds to the tangent point

common to all the leading edges, as depicted in Fig. 1(a). It is worthwhile mentioning that the values for the total drag were obtained by assuming the shapes acting as leading edges. Therefore, no base pressure effects were taken into account on the calculations.

Distributions of pressure drag coefficient C_{pd} , skin friction drag coefficient C_{fd} and total drag coefficient C_d are displayed in Fig. 6 as a function of the power law exponent, with altitude as a parameter. Based on the previous behavior for pressure and skin friction coefficients, the results for drag coefficient tend to confirm the expectation that the total drag coefficient increases with increasing rarefaction. It is found that the major contribution to the total drag coefficient rise is given by the skin friction drag component, which experiences a significant increase in value with increasing the altitude.

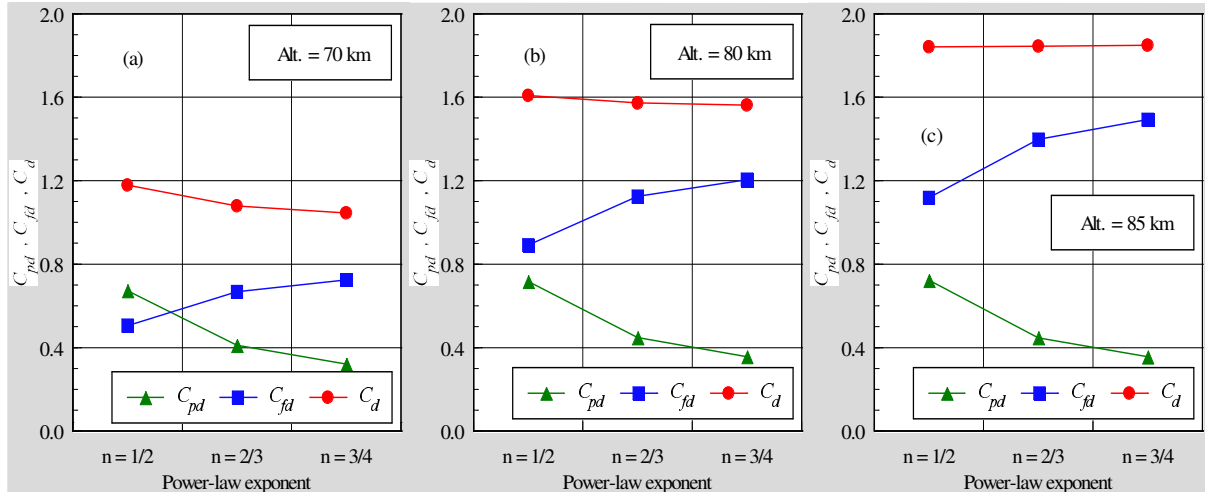


Figure 6: Effect of rarefaction on pressure drag C_{pd} , skin friction drag C_{fd} and total drag coefficient C_d along the power-law body for altitude of (a) 70, (b) 80 and (c) 85 km.

Particular attention is paid to the behavior of pressure and drag contributions displayed in Fig. 6. It is clearly noticed that for blunt leading edge ($n = 1/2$), the pressure drag is larger than that for skin friction drag. In contrast, for sharp leading edge ($n = 3/4$), the pressure drag is smaller than that for skin friction drag.

7. CONCLUDING REMARKS

This study applies the Direct Simulation Monte Carlo method to investigate the aerodynamic surface quantities for a family of power-law leading edges. The calculations have provided information concerning the nature of the number flux, heat transfer, wall pressure, wall shear stress and drag resulting from variations on the power-law exponent and on the altitude for the idealized situation of two-dimensional hypersonic rarefied flow.

The analysis showed that the aerodynamic surface quantities were affected by changes not only on the leading-edge shapes but also on the rarefaction. It was found that the heat transfer coefficient increased at the vicinity of the stagnation region with the altitude rise. Also, it was observed that the total drag enhanced by increasing the altitude.

REFERENCES

Alexander, F. J., Garcia, A. L., & Alder, B. J., 1998, Cell size dependence of transport coefficient in stochastic particle algorithms. *Physics of Fluids*, vol. 10, n. 6, pp. 1540-1542.

- Alexander, F. J., Garcia, A. L., & Alder, B. J., 2000, Erratum: Cell size dependence of transport coefficient is stochastic particle algorithms. *Physics of Fluids*, vol. 12, n. 3, pp. 731-731.
- Anderson, J. L., 1990, Tethered aerothermodynamic research for hypersonic waveriders. *Proceedings of the 1st International Hypersonic Waverider Symposium*, Univ. of Maryland, College Park, MD.
- Bird, G. A., 1981, Monte Carlo simulation in an engineering context. In Sam S. Fisher, ed., *Progress in Astronautics and Aeronautics: Rarefied gas Dynamics*, vol. 74, part I, pp. 239-255, AIAA, New York.
- Bird, G. A., 1989, Perception of numerical method in rarefied gasdynamics. In E. P. Muntz, and D. P. Weaver and D. H. Campbell, eds., *Rarefied gas Dynamics: Theoretical and Computational Techniques*, vol. 118, pp. 374-395, Progress in Astronautics and Aeronautics, AIAA, New York.
- Bird, G. A., 1994, *Molecular Gas Dynamics and the Direct Simulation of Gas Flows*. Oxford University Press, Oxford, England, UK.
- Borgnakke, C. & Larsen, P. S., 1975, Statistical collision model for Monte Carlo simulation of polyatomic gas mixture. *Journal of computational Physics*, vol. 18, n. 4, pp. 405-420.
- Garcia, A. L., & Wagner, W., 2000, Time step truncation error in direct simulation Monte Carlo. *Physics of Fluids*, vol. 12, n. 10, pp. 2621-2633.
- Graves, R. E. & Argrow, B. M., 2001, Aerodynamic performance of an osculating-cones waverider at high altitudes. In *35th AIAA Thermophysics Conference*, AIAA Paper 2001-2960, Anaheim, CA.
- Guo, K. & Liaw, G.-S., 2001, A review: boundary conditions for the DSMC method. In *Proceedings of the 35th AIAA Thermophysics Conference*, AIAA Paper 2001-2953, Anaheim, CA.
- Hadjiconstantinou, N. G., 2000, Analysis of discretization in the direct simulation Monte Carlo. *Physics of Fluids*, vol. 12, n. 10, pp. 2634-2638.
- Mason, W. H. & Lee, J., 1994, Aerodynamically blunt and sharp bodies. *Journal of Spacecraft and Rockets*, vol. 31, n. 3, pp. 378-382.
- Nonweiler, T. R. F., 1959, Aerodynamic problems of manned space vehicles. *Journal of the Royal Aeronautical Society*, vol. 63, Sept, pp. 521-528.
- Potter, J. L. & Rockaway, J. K., 1994, Aerodynamic optimization for hypersonic flight at very high altitudes. In B. D. Shizgal and D. P. Weaver, eds., *Rarefied gas Dynamics: Space Science and Engineering*, vol. 160, pp. 296-307, Progress in Astronautics and Aeronautics, AIAA New York.
- Rault, D. F. G., 1994, Aerodynamic characteristics of a hypersonic viscous optimized waverider at high altitude. *Journal of Spacecraft and Rockets*, vol. 31, n. 5, pp. 719-727.
- Santos, W. F. N. & Lewis, M. J., 2002a, Power law shaped leading edges in rarefied hypersonic flow. *Journal of Spacecraft and Rockets*, vol. 39, n. 6, pp. 917-925.
- Santos, W. F. N. & Lewis, M. J., 2002b, Angle of attack effect on rarefied hypersonic flow over power law shaped leading edges. In *23rd International Symposium on Rarefied Gas Dynamics*, Whistler, BC, Canada.
- Santos, W. F. N. & Lewis, M. J., 2003, Aerodynamic heating performance of power law leading edges in rarefied hypersonic flow. In *36th AIAA Thermophysics Conference*, AIAA Paper 2003--3894, Orlando, FL.
- Santos, W. F. N. & Lewis, M. J., 2004a, Effects of compressibility on rarefied hypersonic flow over power law leading edges. In *42nd AIAA Aerospace Sciences Meeting and Exhibit*, AIAA Paper 2004-1181, Reno, NV.

- Santos, W. F. N. & Lewis, M. J., 2004b, DSMC calculations of rarefied hypersonic flow over power law leading edges with incomplete surface accommodation. In *34th AIAA Fluid Dynamics Conference and Exhibit*, AIAA Paper 2004-2636, Portland, OR.
- Santos, W. F. N. & Lewis, M. J., 2005a, Calculation of shock wave structure over power-law bodies in hypersonic flow. *Journal of Spacecraft and Rockets*, vol. 42, n. 2, pp. 213-222.
- Santos, W. F. N. & Lewis, M. J., 2005b, Aerothermodynamic performance analysis of hypersonic flow on power law leading edges. *Journal of Spacecraft and Rockets*, vol. 42, n. 4, pp. 588-597.
- Santos, W. F. N., 2005, Leading-edge bluntness effects on aerodynamic heating and drag of power-law body in low-density hypersonic flow. *Journal of Brazilian Society of Mechanical Sciences and Engineering*, vol. 27, n. 3, pp. 236-241.
- Shvets, A. I., Voronin, V. I., Blankson, I. M., Khikine, V., & Thomas, L., 2005, On waverider performance with hypersonic flight speed and high altitudes. *43rd AIAA Aerospace Sciences Meeting and Exhibit*, AIAA Paper 2005-0512, Reno, NV.